DUST RADIATIVE EFFECT EXPERIMENTS USING THE LMD MARS GENERAL CIRCULATION MODEL.

Madeleine[1], J.-B., Forget[2], F., Millour[3], E. and Wolff[4], M. J. [1,2,3]Laboratoire de Météorologie Dynamique (LMD), CNRS/UPMC/IPSL, Université Paris 6, BP 99, 4 place Jussieu, 75252 Paris cedex 05, FRANCE ([1]jbmlmd@lmd.jussieu.fr, [2]Francois.Forget@lmd.jussieu.fr, [3]ehouarn.millour@lmd.jussieu.fr). [4]Space Science Institute, 18970 Cavendish Rd, Brookfield, WI 53045, USA (mjwolff@spacescience.org).

1. Introduction: Correctly taking into account the radiative effect of dust in Global Climate Models (GCM) is vital to obtain realistic atmospheric temperature and dynamics. Until now, the radiative transfer of the LMD/GCM was using composite dust radiative properties built on the observations of Ockert-Bell et al., Toon et al. and Clancy and Lee [1,2,3,4]. Since then, new data have allowed a better reconstruction of the dust refractive index, covering the entire solar and thermal infrared spectral range [5,6,7].

On this basis, we have provided the LMD/GCM with new dust radiative properties. For comparison, we ran three simulations, one using the "old" radiative properties (Ockert-Bell et al. 1997) and two using the updated properties of Wolff et al. These two simulations are based on different assumptions: spatially homogeneous scattering parameters on one hand, and size-dependent scattering parameters on the other. It is worth mentioning that clouds are not radiatively active in these experiments. After a short overview of the methods and data used to constrain the model, we will analyze the atmospheric thermal structures in the three cases, compare them to TES observations (through the UK/MGCM reanalysis [8,9]), and discuss our ability to reconcile the LMD/GCM predictions with the available observations both in the visible and infrared ranges.

2. Architecture of the model:

1st simulation ("Ockert-Bell" scattering parameters): The extinction coefficient, single scattering albedo and asymmetry parameter (i.e. single scattering parameters) of the 1st simulation are built upon the analyses of [2] in the GCM solar channels (0.1-5μm), and upon IRIS/Mariner 9 observations [1] in the infrared channels (5-50 μm). These latter properties have been generated using a sample of clay (montmorillonite 219b), and have been adapted for the GCM by removing the unrealistic absorptions at 20 μm created by this mineral [4]. The black curve of Fig. 1 represents, for instance, the resulting single scattering albedo. In this paper, we chose to focus on the Ockert-Bell et al. dust properties, but it is worth mentioning that measurements by Clancy and Lee [3] have been extensively used as well.

The Ockert-Bell et al. dataset merges information from different instruments looking at different locations and times in order to cover the whole visible and near infrared spectral range, but not the thermal infrared. One consequence is that the dust particle size distributions (which control the balance between dust absorption at solar wavelengths and emission in the infrared region) were different for the two domains. Consequently, the ratio of the extinction efficiency (and thus opacity) in the visible to the one in the infrared (later called the "solar over infrared ratio") was set to correct for this bias and merge both datasets. Usually, we used

$$\tau_{0.67\mu m} / \tau_{9\mu m} = 2$$
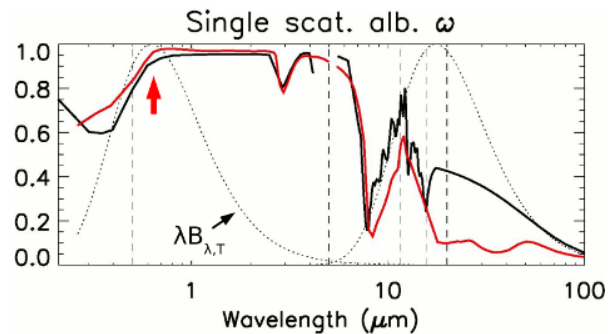
Fig. 1: Dust single scattering albedo measured by [2,4] (black curve) and [6] (red curve). Dashed curves represent the blackbody emission spectra for temperatures of 5870K and 210K, respectively (area preserving representation). Vertical lines show the 6 channels of the GCM radiative transfer scheme.

2nd simulation ("Wolff et al." scattering parameters): Over the last 10 years, many analyses of the dust scattering properties have been conducted at various wavelengths, using TES/MGS [10,5], Mini-TES/MER [11,6], OMEGA/MEx [12,13], CRISM/MRO [7] and MARCI/MRO [14]. In particular, the simultaneous observation of dust in the visible and infrared regions has been done using MGS overflights of the Martian Exploration Rovers [6]. This allows the retrieval of the dust refractive index both in the visible and infrared regions, and avoids the use of an ad hoc solar over infrared ratio as mentioned above. To build the 2nd simulation, we have computed the

dust scattering parameters using the T-Matrix code of M. Mishchenko [15] for a Gamma size distribution (r_{eff}=1.5μm υ_{eff}=0.3) of finite cylinders (D/L=1) [6]. The resulting single scattering albedo is given on Fig. 1 (red curve). We can notice a small difference around 0.7μm (red arrow) between the Ockert-Bell and Wolff et al. single scattering albedo. This is where most of the solar energy lies, and we can thus expect large differences in the predicted heating rates between the 1st and 2nd simulation.

3rd simulation (size-dependent scattering parameters): The dust refractive index can also be used to generate the dust scattering parameters for various dust particle sizes. After storing these scattering parameters in a look-up table, we can thus fully connect, in the GCM, the modeled size distributions to the radiative transfer scheme and let the scattering parameters evolve with the size of the particles. As a first step, we don't carry radiatively active dust explicitly in the model. Rather, we use the size distributions predicted by a separate dust transport experiment (see the paper of F. Forget in this issue). Seasonal variation in the predicted size distributions is shown to be relatively small, and thus, we use for our purpose a fit of the annual mean r_{eff} profile predicted in the dust transport experiment (see Fig. 2) and a constant effective variance (υ_{eff}=0.3). Scattering parameters are then computed in each grid-box by integrating on-line the parameters of the look-up table over a log-normal size distribution.
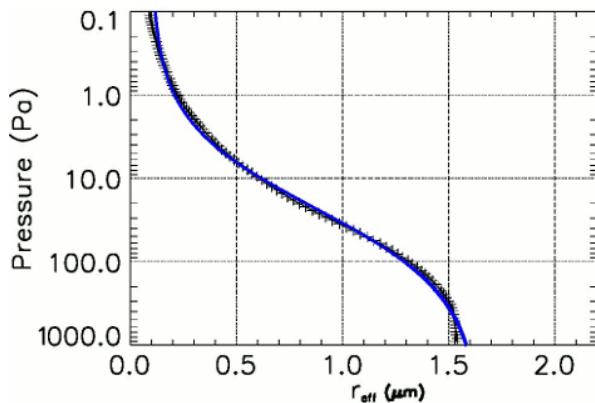
Fig. 2: Fit of the dust annual mean effective radius profile predicted by the dust transport experiment (see the paper by F. Forget in this issue). This analytic function (blue curve) is used to describe the variation in the dust particle size along the vertical in our 3rd simulation, where dust is not carried explicitly by the model.

Dust optical depth: Once the scattering parameters are known, radiative transfer scheme needs the dust optical depth in each layer to finally compute the heating rates. As mentioned above, dust is not carried explicitly by the model in these experiments. Rather, the dust optical depth is deduced by using the space and time varying TES opacity, which corresponds to the total optical depth scaled to an equivalent 6.1 hPa pressure surface [16]. Therefore, the opacity along the vertical axis is computed by weighting the TES opacity with the distribution described in [17] (see [18] for further details):

$$q(z) = q_0 \exp\left(\nu \left[1 - \left(\frac{p_{ref}}{p(z)}\right)^{70/z_{max}} \right] \right)$$

TES opacity is an absorption opacity, and it also has to be converted to an extinction opacity, which is the opacity actually used by the GCM. We use for that the simple relation:

$$\tau_{ext} = \frac{\tau_{abs}}{1 - \omega}$$

Finally, in order to be as close as possible to the observations, the annual mean temperature at 1.06 hPa pressure level predicted by the GCM is compared to the UK/MGCM reanalysis of TES observations. The "input" dust opacity used to constrain the amount of dust in the atmosphere is then multiplied by a tuning factor to approach the observed temperatures. In other words, we slightly change the opacity of the atmosphere to fit the data. One of our goals is to reach a good tuning factor, i.e. to use an opacity that is close to what is really observed by TES, while at the same time predicting good temperatures.

3. Observational dataset:

Atmospheric thermal structure predicted by the LMD/GCM is compared to the reanalysis derived from TES temperature retrievals using the UK/MGCM [8,9]. Figure 3 shows the zonally and time averaged (over 10 days) temperature fields of the reanalysis. The warm perihelion season is clearly distinguished, as well as the comma-shaped temperature inversion in the mid-latitudes, which results from the adiabatic heating of the atmosphere in the descending branch of the Hadley cell.

4. Predicted thermal structures

1st simulation: Top panel of Fig. 4 represents the temperature difference between the LMD/GCM (blue curve) and the UK/MGCM reanalysis of TES observations (red curve) at 1.06 hPa pressure level. The two main differences occur around 30°N and in the north polar region. The first difference is possibly due a

weaker intensity of the Hadley cell in the GCM than observed. The second difference results from the radiative cooling by water ice clouds that is not taken into account in these simulations. The agreement is thus encouraging, since radiatively active clouds will probably improve these results in the future.
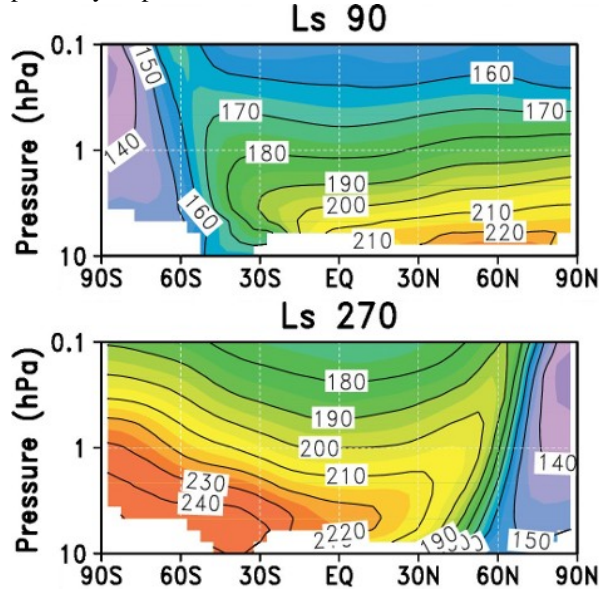
Fig. 3: Zonally and time averaged (over 10 days) temperature fields from the UK/MGCM reanalysis of TES observations [8,9] at two different seasons. This reanalysis is used as a guideline to evaluate the LMD/GCM.

The problem is that the tuning factor corresponds to an opacity equal to 42% of the actual TES opacity. This means that the TES opacity used to constrain the model's dust cycle (see section 2) has to be severely reduced to reach reasonable temperatures. This is a well-known problem due to dust being relatively dark in the Ockert-Bell et al. dataset (see the single scattering albedo in Fig. 1). Therefore, dust absorption at solar wavelengths is too large, and implies too much warming if dust opacity is not artificially reduced to lower values.

2nd simulation: Middle panel of Fig. 4 now represents the same temperature difference when using the Wolff et al. radiative properties. Same difference is noticed in the north polar region, along with a slight improvement in the northern branch of the Hadley cell. But the main improvement is the near disappearance of the tuning factor, which is now close to unity. Indeed, an excellent thermal structure is predicted using 94% of the observed dust opacity. The Wolff et al. dust properties thus allow us to predict good temperatures, while using at the same time realistic values of the dust opacity both in the visible and infrared ranges.

Figure 5 illustrates the zonally and time averaged (over 10 days) temperature difference between the UK/MGCM reanalysis of TES observations (see Fig. 3) and the 2nd GCM simulation, near aphelion (top panel) and perihelion (bottom panel). Radiative effect of water ice clouds (indicated by blue dashed lines and arrows) is prominent. For example, top panel shows a cold bias of the GCM near the equator and at 60°S which is comparable to the one discussed in [20] (see Fig. 3c therein).
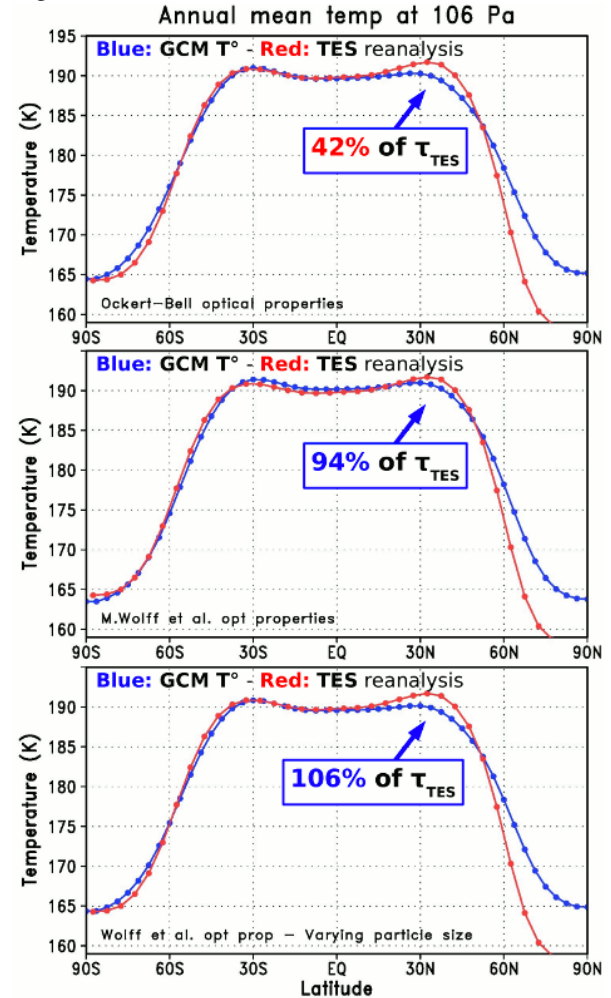
Fig. 4: Zonally and time averaged (over one year) temperature at 1.06 hPa pressure level from TES reanalysis (red curve) and as predicted by the LMD/GCM (blue curve) for three different cases: a simulation using the Ockert-Bell radiative properties (**top panel**), another simulation using the Wolff et al. properties (**middle panel)** and a last simulation that uses size-dependent scattering parameters (**bottom panel)**. The 1.06 hPa pressure level is chosen because of its proximity to the peak of the weighting function for the 15μm CO_2 band [19].

Similarly, warm biases in the mid-latitudes and polar regions are likely due to water ice clouds (see arrows in Fig. 5). Significant differences are seen at the north pole for $L_s=270°$ (0.1 hPa level, bottom panel), but it is difficult to know whether the reanalysis or the GCM is right in these regions that are strongly dynamically controlled, and further analysis is necessary.

Apart from these differences, the overall agreement is really satisfying. The next step is to account for size-dependent scattering parameters.

Ls 90

Ls 270
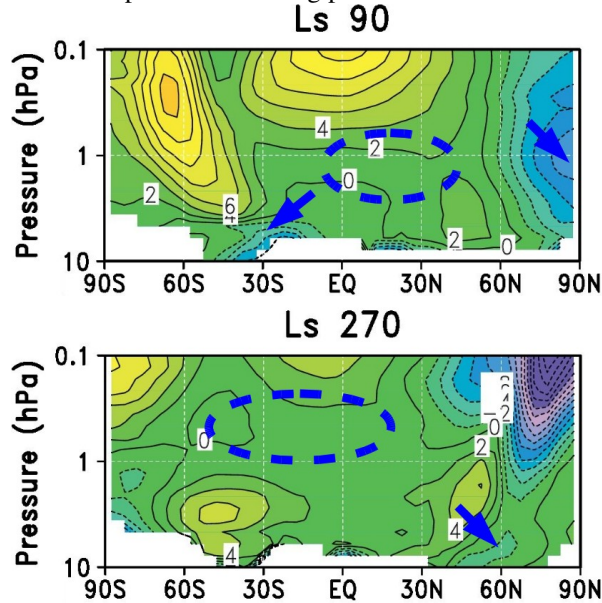
Fig. 5, T_{TES}-T_{GCM}: Temperature difference between the UK/MGCM reanalysis of TES observations and our 2nd simulation (Wolff et al. radiative properties and homogeneous scattering parameters). Contour interval is 2K. Blue dashed lines and arrows indicate the approximate location of water ice clouds.

3rd simulation: In this last simulation, scattering parameters are varying as a function of dust particle size. As seen in Fig. 4 (bottom panel), the observed temperature at 1.06 hPa pressure level can be well reproduced again using a realistic dust opacity.

Figure 6 illustrates the zonal mean temperature difference between the UK/MGCM reanalysis of TES observations and our simulation. When comparing Fig. 6 to the bottom panel of Fig. 5, we can see that most of the changes occur, as expected, at high altitude, where dust particles are smaller. The scattering parameters being now size-dependent, these particles have a smaller absorption at solar wavelengths, and the atmosphere is colder than in the 2nd simulation around the 0.1 hPa pressure level. Therefore, the equatorial and polar cold and warm biases are respectively more and less pronounced. Adding radiatively active

water ice clouds is the next necessary step to further understand these biases.

Ls 270
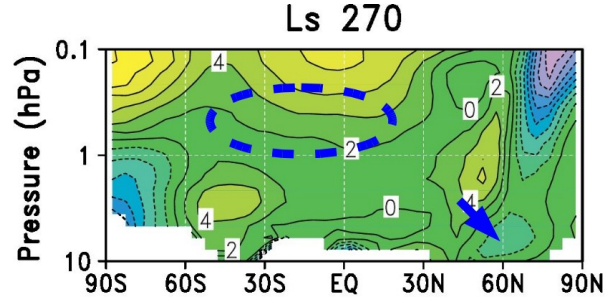
Fig. 6: Same as Fig. 5, but using 3D size-dependent scattering parameters.

5. Conclusion

Dust radiative properties have been updated in the LMD/GCM using homogeneous and size-dependent scattering parameters, and main results can be summarized as follows:

• The use of the new Wolff et al. radiative properties results in a good thermal structure, while being at the same time consistent with the observed visible and infrared opacities. This was not the case for previous radiative properties and versions of the model;

• Taking into account the size-dependence of the dust scattering parameters has a significant impact on the GCM temperatures, especially at high altitude;

• Adding radiatively active clouds is the next necessary step to clarify the origin of the remaining differences between the LMD/GCM results and the UK/MGCM reanalysis of TES observations.

[1] Toon, O. B. et al. (1977) *Icarus 30*, 663-696. [2] Ockert-Bell, M. E. et al. (1997) *JGR 102*, 9039-9050. [3] Clancy, R. T. and Lee, S. W. (1991) Icarus 93, 135-158. [4] Forget, F. (1998) *GRL 25*, 1105-1108. [5] Wolff, M. J. and Clancy, R. T. (2003) *JGR (Planets) 108*, E9, 5097. [6] Wolff, M. J. et al. (2006) *JGR (Planets) 111*, E12S17. [7] Wolff, M. J. et al. (2009) *JGR (Planets) 114*, E00D04. [8] Lewis, S. R. et al. (2007) *Icarus 192*, 327-347. [9] Lewis, S. R. et al. (2008) *Third Int. Workshop on The Mars Atmosphere*, LPI Contribution n°1447, Abstract 9009. [10] Clancy, R. T. et al. (2003) *JGR (Planets) 108*, E9, 5098. [11] Smith, M. D. et al. (2006) *JGR (Planets) 111*, E12S13. [12] Vincendon, M. et al. (2007) *JGR (Planets) 112*, E08S13. [13] Määttänen, A. et al. (2009) *Icarus 201*, 504-516. [14] Wolff, M. J. et al. (2007) *7th Int. Conf. on Mars*, Abstract #3121. [15] Mishchenko, M. I. et al. (1996) *J. Quant. Spectrosc. Radiat. Transfer, vol. 55*, 535-575. [16] Smith M. D. et al. (2004) *Icarus 167*, 148-165. [17] Forget, F. et al. (1999) *JGR 104*, 24155-24176. [18] Montmessin, F. et al. (2004) *JGR (Planets) 109*, 10004. [19] Conrath, B. J. et al. (2000) *JGR 105*, 9509-9520. [20] Wilson, R. J. et al. (2008) *GRL 35*, 7202.